 

*THZ RADIATION*

https://doi.org/10.1070/QEL16694

# Comparative analysis of 2D spatio-temporal visualisation techniques for the pulsed THz-radiation field using an electro-optic crystal

A.A. Ushakov, P.A. Chizhov, V.V. Bukin, S.V. Garnov, A.B. Savel'ev

***Abstract.*** **Two 2D techniques for visualising the field of pulsed THz radiation ('shadow' and 'interferometric'), which are based on the linear electro-optical effect with application of a ZnTe detector crystal 1×1 cm in size, are compared. The noise level and dynamic range for the aforementioned techniques are analysed and their applicability limits are discussed.**

***Keywords:*** *THz radiation, interferometry, electro-optic detection.*

## 1. Introduction

Active development of THz radiation sources opens ways for new applications in spectroscopy, microscopy, remote sensisng, tomography, and imaging [1–12]. Pulsed THz sources are of particular interest. They are used to solve various problems of time-domain spectroscopy, e. g., by applying electro-optic detection [4, 5, 12]. There are different schemes for detecting pulsed THz-radiation fields using electro-optic crystals. The pioneer studies in this area [2, 4] were performed using detectors without spatial resolution, as a result of which it was necessary to apply raster scanning. In addition, the visualisation rate decreased because of the scanning of the delay between the probe optical and THz pulses. The latter hindrance was overcome by applying chirped probe pulses, which allow one to detect the temporal shape of a THz pulse [6, 13, 14]. However, the visualisation rate is mainly determined by the time necessary for spatial scanning [7, 15]. Therefore, it is of interest to use crystals with a large aperture [16–19] to visualise a THz pulse without spatial scanning.

Currently, there are two techniques for visualising THz pulse fields with application of wide-aperture electro-optic crystals, which make it possible to exclude point-to-point spatial scanning. The first technique (which will be referred to as shadow below) is based on recording small variations in the probe beam intensity due to the depolarisation induced by the THz field in the electro-optic crystal. This technique was demonstrated when recording the THz pulse field using partially crossed polarisers in the detector [18, 19] or squared THz pulse field using crossed polarisers in the detector [7]. The second technique, which will be referred to as interferometric, is based on recording the interference fringe bending caused by the birefringence induced by the THz field in an electro-optic crystal [17]. In this work, we compare these two schemes for visualising the THz pulse field by applying a wide-aperture electro-optic crystal, which allow one to exclude point-to-point scanning.

**A.A. Ushakov** A.M. Prokhorov General Physics Institute, Russian Academy of Sciences, ul. Vavilova 38, 119991 Moscow, Russia; Faculty of Physics, M.V. Lomonosov Moscow State University, Vorob'evy gory, 119991 Moscow, Russia; e-mail: ushakov.aleksandr@physics.msu.ru;
**P.A. Chizhov, V.V. Bukin, S.V. Garnov** A.M. Prokhorov General Physics Institute, Russian Academy of Sciences, ul. Vavilova 38, 119991 Moscow, Russia;
**A.B. Savel'ev** Faculty of Physics, M.V. Lomonosov Moscow State University, Vorob'evy gory, 119991 Moscow, Russia

Received 5 April 2018
*Kvantovaya Elektronika* **48** (5) 487–490 (2018)
Translated by Yu.P. Sin'kov

## 2. Experimental setups

### 2.1. Schematic of measuring the THz field by the shadow method on setup 1

The light source was a Ti:sapphire laser (centre wavelength 775 nm, pulse repetition rate 10 Hz, pulse duration 150 fs, pulse energy 2.8 mJ, Gaussian beam diameter 12 mm at the $1/e^2$ level, horizontal polarisation). The laser radiation was split into two beams. The main part was applied to generate THz radiation in the source (Fig. 1); this generation is based on optical rectification of femtosecond radiation with a tilted intensity front in a lithium niobate ($LiNbO_3$) crystal [20]. The THz radiation from the source was collimated and focused by two

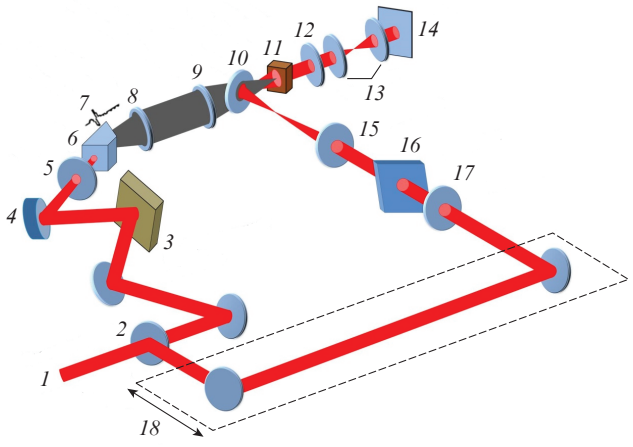


**Figure 1.** Schematic of setup 1:
(*1*) Ti:sapphire laser (775 nm, 10 Hz, 2.8 mJ); (*2*) beam splitter; (*3*) grating; (*4*) spherical mirror ($f$ = 20 cm); (*5*) $\lambda/2$ plate; (*6*) $LiNbO_3$ crystal; (*7*) THz radiation; (*8*) PTFE lens ($f$ = 10 cm); (*9*) PTFE lens ($f$ = 6 cm); (*10*) pellicle beamsplitter; (*11*) ZnTe crystal (0.5 mm); (*12*) polariser; (*13*) telescope; (*14*) CMOS camera; (*15*) lens ($f$ = 5 cm); (*16*) filters; (*17*) $\lambda/4$ plate; (*18*) delay line.

PTFE lenses with focal lengths $f$ = 10 and 6 cm onto the surface of a wide-aperture ZnTe detector crystal (10 × 10 × 0.5 mm, orientation <110>). The rest of the laser radiation (probe pulse) was transmitted through a variable optical delay line, a quarter-wave plate, light filters, and a beam-expanding lens, after which it was aligned with the THz beam on a pellicle beamsplitter and directed to the ZnTe crystal. The plane of the ZnTe detector crystal was reflected by a telescope onto the CMOS camera array (Basler acA2040–25gm-NIR, 1″, 2048 × 2048). A polariser transmitting vertically polarised radiation was introduced in the path of the probe beam to the telescope. The THz field induced birefringence in the crystal and changed the brightness of crystal image in the CMOS camera due to the linear electro-optic effect [21].

The brightness of the crystal surface image varied due to the electro-optic effect [1] proportionally to the light phase shift induced by the THz field:

$$I \cong \frac{I_0}{2}\left(1 + \frac{\pi E_{\mathrm{THz}}}{E_\pi}\right). \qquad (1)$$

Here, $E_{\mathrm{THz}}$ is the THz electric field strength; $E_\pi$ is the THz field strength causing a phase shift by π; and $I_0$ is the initial optical beam intensity. For the ZnTe crystal in use, $E_\pi$ = 178 kV cm$^{-1}$ [1]. Typical values of observed field strengths in setup 1 were 2–3 kV cm$^{-1}$; hence, linear approximation (1) can be used in this case. Thereafter, 2D distributions of THz field amplitude could be found from the patterns of crystal surface illuminance. Changing the delay between the THz and optical pulses, one could obtain a 2D–temporal (2D + $\tau$) distribution of THz electric field.

During the experiment, to increase the signal-to-noise ratio, we obtained crystal images both in the presence of the THz field and in the absence of the field (signal and reference images, respectively). Fifty signal and reference frames were obtained for each position of the time delay between the optical and THz pulses. First, the signal and reference images were averaged independently and separately for each delay. Since the THz field strength is proportional to the relative change in the brightness of crystal surface image due to the electro-optic effect, we used a reference series of images in order to take into account the change in the image brightness with respect to the initially unperturbed light. Thus, the THz field value can be calculated by the formula

$$E_{\mathrm{THz}}(x,y,\tau) = \frac{I_{\mathrm{sign}}(x,y,\tau) - I_{\mathrm{ref}}(x,y,\tau)}{I_{\mathrm{ref}}(x,y,\tau)}\,\frac{E_\pi}{\pi}$$

$$= \frac{I_{\mathrm{sign}}(x,y,\tau) - I_{\mathrm{ref}}(x,y,\tau)}{I_{\mathrm{ref}}(x,y,\tau)} \times 55\ \mathrm{kV\ cm^{-1}}, \qquad (2)$$

where $I_{\mathrm{sign}}(x,y,\tau)$ and $I_{\mathrm{ref}}(x,y,\tau)$ are, respectively, the signal and reference image intensities at different points of the crystal surface (coordinates $x,y$) and at different delay times $\tau$ between the optical and THz pulses. Thus, we obtained a 3D data array: a set consisting of about 100 2D images (2048 × 2048 points in each), with a time step of 125 fs. Since the image pixel size is 5.5 μm, i.e., a value much smaller than the characteristic THz wavelength (a frequency of 0.6 THz in the source spectrum maximum corresponds to a wavelength of 400 μm), the initial image size (2048 × 2048 pixels) is redundant. Spatial filtering using a Gaussian filter ($\sigma$ = 60 μm) with subsequent coarsening of the thus obtained effective pixels of distributions was used to reduce the amount of data. The final size of spatial distributions was 120 × 120 points.

### 2.2. Schematic of measuring the THz field by the interferometric method on setup 2

The second scheme (Fig. 2) also used a Ti:sapphire laser (800 nm, 10 Hz, 40 fs, 2.5 mJ, 12 mm at the level of 1/e$^2$, horizontal polarisation). As in the above-described setup, THz radiation was detected according to the pump–probe scheme. The main part of the light beam was used to pump the THz radiation source, as well as for the source in setup 1. The rest of the laser beam (probe pulse) detected the field by means of the interferometric technique. The detector crystal plane was imaged by a telescope onto the matrix of the same CMOS camera. The interferometer consisted of two Wollaston prisms (with beam separation angles of 1.5° and 3°) and a polariser (oriented at an angle of 45°). The THz field visualisation was based on the registration of the variations in the interference pattern due to the change in the optical path length for waves with orthogonal polarisations as a result of the birefringence induced in the crystal under an external THz field. The principle of measuring the THz field was described in detail in [17].

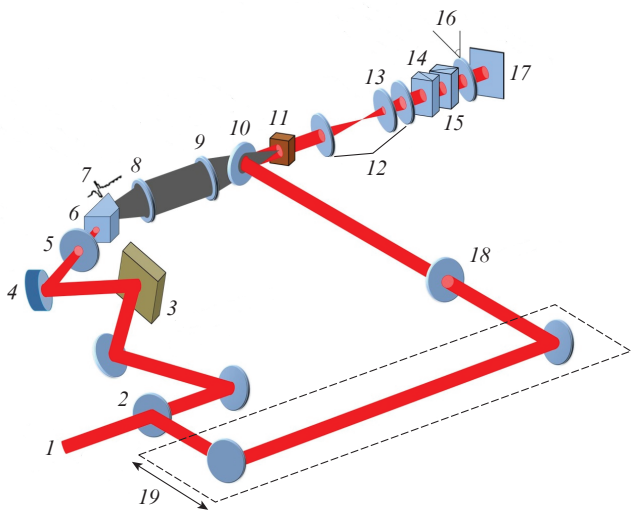


**Figure 2.** Schematic of setup 2:
(*1*) Ti:sapphire laser (800 nm, 10 Hz, 2.5 mJ); (*2*) beam splitter; (*3*) grating; (*4*) spherical mirror ($f$ = 20 cm); (*5*) $\lambda/2$ plate; (*6*) $LiNbO_3$ crystal; (*7*) THz radiation; (*8*) PTFE lens ($f$ = 10 cm); (*9*) PTFE lens ($f$ = 6 cm); (*10*) pellicle beamsplitter; (*11*) ZnTe crystal (0.5 mm); (*12*) telescope; (*13*) interference filter; (*14*) Wollaston prism ($\alpha$ = 1.5°); (*15*) Wollaston prism ($\alpha$ = 3°); (*16*) polariser ($\beta$ = 45°); (*17*) CMOS camera; (*18*) $\lambda/2$ plate; (*19*) delay line.

Similar to the above-described method, we obtained images of the electro-optic crystal surface with interference fringes (interference patterns) both in the presence of a THz pulse and without it (signal and reference patterns, respectively). To increase the signal-to-noise ratio, we also made 50 signal and reference frames for each delay between the optical and THz pulses. The phase difference was recovered by processing interference patterns based on the Fourier space filtering method [22]; thereafter, the thus obtained phase distributions were averaged. The processing yielded a 2D distribution of the mean

variation in the phase shift due to the presence of THz pulse field. Based on the phase shift, one can calculate the THz field strength $E_{THz}$. According to [23], when the polarisations of optical and THz pulses are oriented relative to the ZnTe crystallographic axes in the same way as in our experiment,

$$E_{THz} = \frac{\Gamma\lambda}{\pi d n^3 r_{41}} = \frac{\Gamma E_\pi}{\pi} \cong \Gamma \times 55 \text{ kV cm}^{-1}, \quad (3)$$

where $\Gamma$ is the phase shift induced by the THz field; $\lambda$ is the laser wavelength; $n$ and $r_{41}$ are, respectively, the refractive index and electro-optic coefficient of the crystal; and $d$ is the crystal thickness.

## 3. Experimental results

Thus, we obtained a number of sets of 2D spatial distributions of THz pulse electric fields, measured by both the shadow (Fig. 3) and interferometric (Fig. 4) techniques. Since the optical pulse is much shorter than the THz pulse, the field of the latter can be considered as constant in comparison with the optical field. There is synchronism between the THz radiation and light in the crystal; therefore, the THz field can be considered as constant throughout the entire volume. Light was incident normally on the crystal in both experimental schemes; therefore, the recorded field distributions are cross sections of THz pulse wavefronts by the optical pulse front, which coincides with the crystal plane.

In the shadow technique, under conditions of normal incidence of THz radiation with a plane wave front, one should observe darkening or lightening of the entire image with a change in the delay between the optical and THz pulses. In the case of an obliquely incident plane THz wavefront, the cuts of THz pulse wavefronts will be presented by fringes corresponding to the field strengths, moving along the crystal plane with a change in the delay between the optical and THz pulses. The closer the angle of incidence to normal, the wider these fringes are.

The aberration and diffraction effects during propagation of THz pulses lead to bending of their wavefronts and corresponding bending of fringes in the distributions recorded. In our case the angles of incidence of THz radiation relative to the crystal plane and, therefore, to the plane of probe wavefront in the above-described setups were different, which led to different fringes in the spatial distributions of obtained THz fields: the fringes observed in the interference technique are much narrower than those in the shadow technique. Fringes are shifted with a change in the delay between the probe and THz pulses. Zero delay in Figs 3 and 4 was chosen arbitrarily for the following reason: to analyse the THz pulse wavefront, it is important to know only the relative change in the delay between the optical and THz pulses.

To estimate the noise component in the field distributions, we calculated the rms data in the frame region where the signal was absent. In the shadow technique, the equivalent value of field strength noise $\delta E$ was 100 V cm$^{-1}$. In the interferometric method, the rms value of the phase difference noise component was 5 mrad, which is equivalent to the electric field strength noise $\delta E$ = 280 V cm$^{-1}$. The aforementioned values are in agreement with the previous experimental data [6, 7, 17, 23]. One of the main reasons for the decrease in sensitivity in the interference method is the existence of mechanical vibrations, which cause a random shift of interference fringes in the detector crystal plane. This drawback can be eliminated by attenuating mechanical vibrations and increasing the number of image averagings.

An important characteristic of the methods in use is their dynamic measurement range. It is defined as the ratio of the maximum measured THz field strength to the rms noise level. The maximum measurement range of the THz field in electro-optic techniques is primarily determined by the detector crystal properties (electro-optic coefficient, orientation of axes, thickness). The same ZnTe crystal was applied in both experimental schemes. The maximum measured field value in both schemes is $E_\pi$ = ±178 kV cm, which corresponds to attainment of maximum/minimum brightness of the crystal image in the shadow technique or half-fringe shift in interference pattern. This, in turn, corresponds to the boundaries of the domain of unambiguous phase determination in the interference technique. The dynamic range for the shadow and interference techniques was, respectively, 1780 and 636. The main advantage of the latter approach is that, in contrast to the

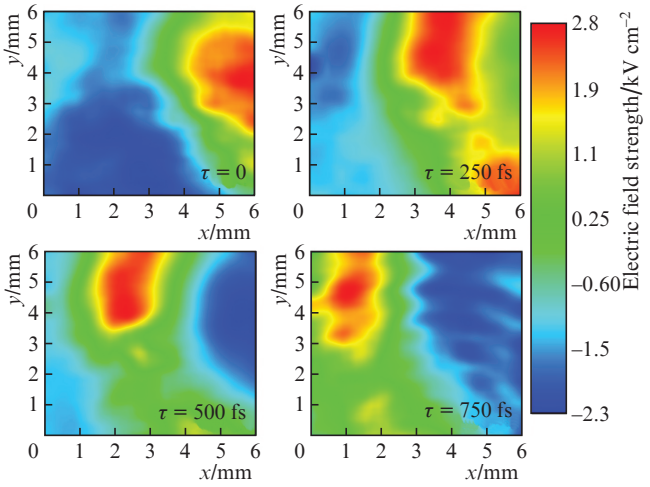


**Figure 3.** (Colour online) Spatial distributions of the THz radiation field, obtained using the shadow technique at different time delays $\tau$ between the probe optical and THz pulses.

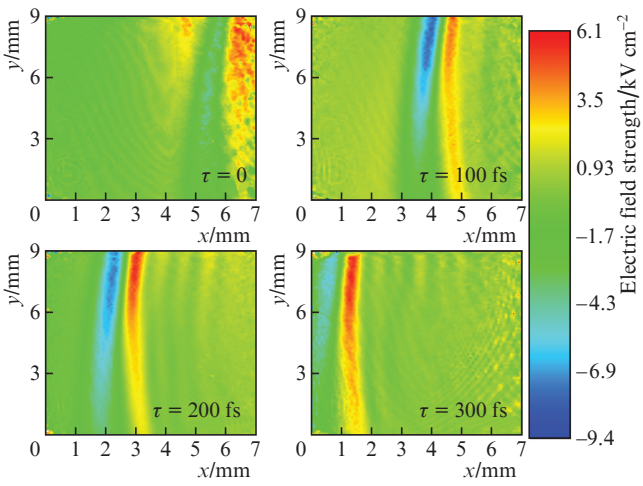


**Figure 4.** (Colour online) Spatial distributions of the THz radiation field, obtained using the interferometric technique at different time delays $\tau$ between probe optical and THz pulses.

shadow technique, it deals with the interference fringe contrast rather than with the frame illuminance. When the brightness of the crystal plane image changes (as a result of probe beam displacement in the crystal plane or due to illuminance fluctuations in different frame areas), the noise level for the shadow technique increases, whereas the influence of this effect for the interference technique is much weaker. However, this advantage of the interference technique before the shadow method disappears when the probe beam quality is characterised by high reproducibility.

Another important issue is the linear dependence of the response signal on the THz field strength. Formulas (1)–(3) were derived on the assumption that the response to the THz field is linear; it is not correct to use them for the fields obtained in the last studies [24–26]. Other methods should be used to estimate such fields.

## 4. Conclusions

Two schemes for visualising THz pulse fields, based on measuring the depolarisation of a probe laser pulse in an electro-optic crystal by shadow and interferometric methods, were compared. The presence of mechanical vibrations in the interferometric scheme resulted in a three times as large noise level and three times as small dynamic measurement range as compared with the shadow technique. The interferometric technique may be advantageous for visualising THz fields when applying laser systems with small-scale fluctuations of beam intensity and directionality. Although both techniques have a limited range of measuring the THz field strength, they do not require point-to-point scanning and can be used to construct object images in the THz range.

***Acknowledgements.*** This work was supported by the Presidium of the Russian Academy of Sciences ('Extreme Laser Radiation: Physics and Fundamental Applications Programme). A.A. Ushakov acknowledges the support of the Foundation for Assistance to Small Innovative Enterprises (Programme 'UMNIK', contract FASIE 11488GU/2017) and the Foundation 'Basis'.

## References

1. Zhang X.-C., Xu J. *Introduction to THz Wave Photonics* (New York: Springer, 2010).
2. Mittleman D.M., Hunsche S., Boivin L., Nuss M.C. *Opt. Lett.*, **22**, 904 (1997).
3. Wynne K., Jaroszynski D. *Opt. Lett.*, **24**, 25 (1999).
4. Mittleman D.M., Jacobsen R.H., Nuss M.C. *IEEE J. Sel. Top. Quantum Electron.*, **2**, 679 (1996).
5. Peiponen K.-E., Zeitler J.A., Kuwata-Gonokami M. (Eds) *Terahertz Spectroscopy and Imaging* (Berlin: Springer-Verlag Berlin Heidelberg, 2013) Vol. 171.
6. Jiang Z., Zhang X. *IEEE J. Quantum Electron.*, **36**, 1214 (2000).
7. Jiang Z., Zhang X. *IEEE Trans. Microw. Theory Tech.*, **47**, 2644 (1999).
8. Oh S.J., Choi J., Maeng I., Park J.Y., Lee K., Huh Y.-M., Suh J.-S., Haam S., Son J.-H. *Opt. Express*, **19**, 4009 (2011).
9. Ferguson B., Wang S., Gray D., Abbot D., Zhang X.-C. *Opt. Lett.*, **27**, 1312 (2002).
10. Hu B.B., Nuss M.C. *Opt. Lett.*, **20**, 1716 (1995).
11. Kim K.Y., Yellampalle B., Taylor J., Rodriguez G., Glownia J.H. *Opt. Lett.*, **32**, 1968 (2007).
12. Wang S., Ferguson B., Abbott D., Zhang X.-C. *J. Biol. Phys.*, **29**, 247 (2003).
13. Yellampalle B., Kim K.Y., Rodriguez G., Glownia J.H., Taylor A.J. *Appl. Phys. Lett.*, **87**, 211109-1 (2005).
14. Jiang Z., Zhang X.-C. *Opt. Lett.*, **23**, 1114 (1998).
15. Kim K.Y., Yellampalle B., Rodriguez G., Averitt R.D., Taylor J., Glownia J.H. *Appl. Phys. Lett.*, **88**, 41123 (2006).
16. Zhang L., Karpowicz N., Zhang C., Zhao Y., Zhang X. *Opt. Commun.*, **281**, 1473 (2008).
17. Chizhov P.A., Ushakov A.A., Bukin V.V., Garnov S.V. *Quantum Electron.*, **45**, 434 (2015) [*Kvantovaya Elektron.*, **45**, 434 (2015)].
18. Wu Q., Hewitt T.D., Zhang X.C. *Appl. Phys. Lett.*, **69**, 1026 (1996).
19. Wu Q., Sun F.G., Campbell P., Zhang X.C. *Appl. Phys. Lett.*, **68**, 3224 (1996).
20. Hebling J., Yeh K.-L., Hoffmann M.C., Bartal B., Nelson K. *J. Opt. Soc. Am. B*, **25**, B6 (2008).
21. Jiang Z., Zhang X.-C. *Opt. Express*, **5**, 243 (1999).
22. Takeda M., Ina H., Kobayashi S. *J. Opt. Soc. Am.*, **72**, 156 (1982).
23. Casalbuoni S., Schlarb H., Schmidt B., Schmüser P., Steffen B., Winter A. *Phys. Rev. Spec. Top. Accel. Beams*, **11**, 1 (2008).
24. Vicario C., Ovchinnikov A.V., Ashitkov S.I., Agranat M.B., Fortov V.E., Hauri C.P. *Opt. Lett.*, **39**, 6632 (2014).
25. Agranat M.B., Chefonov O.V., Ovchinnikov A.V., Ashitkov S.I., Fortov V.E., Kondratenko P.S. *Phys. Rev. Lett.*, **120**, 85704 (2018).
26. Vicario C., Shalaby M., Hauri C.P. *Phys. Rev. Lett.*, **118**, 83901-1 (2017).